Article

Efficient Photocatalytic Degradation of RhB by Constructing Sn₃O₄ Nanoflakes on Sulfur-Doped NaTaO₃ Nanocubes

Sujie Chang [1,*] **, Yuanhua Sang** [2] **and Hong Liu** [2]

[1] School of Materials Science and Engineering, Shandong Jianzhu University, Fengming Road, Jinan 250101, China
[2] State Key Laboratory of Crystal Materials, Shandong University, Jinan 250100, China;
sangyh@sdu.edu.cn (Y.S.); hongliu@sdu.edu.cn (H.L.)
* Correspondence: 13771@sdjzu.edu.cn; Tel.: +86-150-9879-5090

Abstract: Band structure engineering and heterojunction photocatalyst construction are efficient approaches to improve the separation of photo-induced electrons and holes, along with enhancing light response ability. By sulfur doping, sodium tantalite ($NaTaO_3$) showed an improved photocatalytic property for the degradation of Rhodamine B (RhB). Sn_3O_4 nanoflakes were constructed on the surface of $NaTaO_3$ nanocubes, forming a surface heterostructure via a simple hydrothermal process, initially. This heterostructure endows the photocatalyst with an enhanced charge separation rate, resulting in an improved photocatalytic degradation of RhB. Moreover, a possible mechanism over $Sn_3O_4/NaTaO_3$ and the photodegradation pathway of RhB were proposed as the combined effect of photo-induced electrons and holes. This facile process for band structure engineering and heterostructure construction provides the possibility for the practical application of high-efficiency photocatalysts.

---

1. Introduction

In recent years, the extensive treatment of wastewater containing organic pollutants has led to a negative impact on the environment and serious consequences for human health. Although considerable efforts and strategies have been taken to alleviate the above-mentioned problems, the photocatalytic oxidation of water as an advanced sewage disposal mechanism is of confocal interest and is considered an effective solution [1–7]. For this reason, there has been an upsurge in research on a variety of photocatalysts. Among these, ABO_3 perovskite-type oxides have been widely studied, due to their high performance in photocatalytic reactions, such as with overall water splitting and the photodegradation of organic pollutants, which provide a potential approach to solve our urgent energy and environmental problems [8,9]. Sodium tantalite ($NaTaO_3$) is a prominent ABO_3 perovskite-like oxide with a high performance in photocatalytic reactions, including abundance, photochemical stability, photodegradation of organic pollutants, water splitting, and low environmental impact, which attracts a lot of attention for its favorable layered structure and distinctive separation effectiveness in charge separation [10–20]. Hence, $NaTaO_3$-based photocatalysts can intrinsically decrease the recombination rate of photo-induced carriers and promote the efficiency of photocatalytic systems. It has been well-documented that tantalates are superior to other metal oxides. Moreover, $NaTaO_3$ is a new type of wide bandgap semiconductor material, which has a bandgap of about 4.0 eV at room temperature [10]. To enhance the photocatalytic performance, metal or non-metal ions doped with $NaTaO_3$ (dopants: Sr^{2+} [15,17], La^{3+} [20,21], Ba^{2+} [22], Ca^{2+} [23], N or S [12,23]) or semiconductors loaded on $NaTaO_3$, such In_2S_3 [10], WO_3 [11], NiO [24], $AgCl/Ag_2O$ [25], g-C_3N_4 [18,26], RuO_2 [27], and CdS [28] have been typically studied. These works were developed to improve the photocatalytic activity of $NaTaO_3$-based materials. The assessment of composite photocatalysts included photocatalytic water splitting and photodegradation of organic pollutants.

These techniques and other strategies make $NaTaO_3$ a better photocatalyst. Concerning the aforementioned, the potentiality of $NaTaO_3$-based photocatalysts is apparent.

To date, heterovalent tin oxide Sn_3O_4 formed of mixed valences of Sn^{2+} and Sn^{4+} has garnered noticeable attention. One third of Sn atoms are located in Sn (II) tetrahedral coordination sites and two-thirds are located in Sn (IV) octahedral sites [29–31]. Additionally, the Sn_3O_4 tin structure has been reported to influence the physical properties of tin oxide. As proposed by theoretical calculations, Sn_3O_4 has been experimentally confirmed to possess absorption bands in a limited visible-light region, which may have promising applications as a potential photocatalyst in environmental remediation and energy conversion. With a direct bandgap energy of around 2.56 eV, Sn_3O_4 has also been widely studied for its relatively negative conduction band edge and moderate charge transport features. The proper energy band makes it a better material for constructing heterojunction catalysts with other semiconductor materials [32–37]. Hence, it is very vital to broaden the photocatalytic active spectral range and improve the separation of carriers of Sn_3O_4.

To the best of our knowledge, there is no research on the photocatalytic performance of the $Sn_3O_4/NaTaO_3$ heterostructure. Therefore, in the current work, sulfur-doped $NaTaO_3$ cubes were synthesized to modify the band structure of $NaTaO_3$. Based on the appropriate valance band (EVB ~3.01 eV) and conduction band edge (ECB ~0.99 eV) of $NaTaO_3$ [12,28], which can match well with that of Sn_3O_4 (EVB ~1.07 eV and ECB ~1.55 eV vs. NHE, pH = 7) [30], the heterojunction of $Sn_3O_4/NaTaO_3$ was synthesized. An enhanced photo-induced charge separation was highly expected, which results in the enhanced photocatalytic degradation of RhB. This work provides an ordinary and low-cost method for the large-scale production of $NaTaO_3$-based materials in various applications. It is expected to offer an upfront approach for developing highly stable and effective heterostructures for organic pollutant degradation.

2. Materials and Methods

2.1. Materials

Tantalum oxide (Ta_2O_5), hydrochloric acid (HCl), sulfuric acid (H_2SO_4), sodium hydroxide (NaOH), tin(II) chloride dehydrate ($SnCl_2 \cdot 2H_2O$), ethanol (C_2H_5OH), sodium citrate dihydrate ($Na_3C_6H_5O_7 \cdot 2H_2O$), and Rhodamine B (RhB) were purchased from Sinopharm Chemical Reagent Co., Ltd. and used without any further purification. Deionized water was used throughout the study.

2.2. Synthesis

$NaTaO_3$ and sulfur anion doped in $NaTaO_3$ were prepared via the reported effortless hydrothermal approach. In a typical synthesis process, 0.442 g of Ta_2O_5, 1.2 g of NaOH, and a certain amount of $Na_2S_2O_3 \cdot 5H_2O$ were added into a Teflon-lined stainless steel autoclave (50 mL capacity) that was filled with deionized water to 75% of the total volume. The autoclave was sealed and put into a preheated oven to perform hydrothermal treatment at 180 °C for 12 h. After cooling to room temperature, the acquired precipitates were collected by centrifugation and thoroughly washed with deionized water several times, and then dried at 80 °C for 12 h before further characterization and photocatalytic reaction. The obtained products were $NaTaO_3$ powders and S-doped $NaTaO_3$ powders, respectively; the latter had a calculated S:Ta molar ratio of 5%, where the amount of $Na_2S_2O_3 \bullet 5H_2O$ was 0.0248 g.

The $Sn_3O_4/NaTaO_3$ and $Sn_3O_4/NaTaO_3$-S were prepared via a facile hydrothermal co-precipitation method. First, 5.0 mmol of $SnCl_2 \bullet 2H_2O$ and 12.5 mmol of $Na_3C_6H_5O_7 \bullet 2H_2O$ were dissolved in 12.5 mL of deionized water and stirred for 5 min to get a transparent solution, where a certain amount of $NaTaO_3$ or $NaTaO_3$-S (0.175 g) was added. Then, 12.5 mL of 0.2 M NaOH aqueous solution was added to the above-mentioned solution, with vigorous stirring followed by ultrasonic treatment and the solution was transferred to a 50 mL Teflon-lined stainless steel autoclave and maintained at 180 °C for 12 h. The acquired powder was washed with deionized water and ethanol several times and then

finally dried at 60 °C for 12 h. Sn_3O_4/$NaTaO_3$ and Sn_3O_4/$NaTaO_3$-S composites were pre-pared with the molar ratio of Sn:Ta 1:1. Pure Sn_3O_4 was synthesized without the addition of cubic $NaTaO_3$ in a similar process.

The samples acquired above are denoted as $NaTaO_3$, NTO-S, Sn/NTO, Sn/NTO-S, and Sn_3O_4, respectively.

2.3. Characterizations

The crystalline structures of the products were characterized by X-ray diffraction (XRD) on a Bruker D8 Advance powder X-ray diffractometer with Cu Kα radiation (λ = 0.15406 nm). The morphologies of the as-obtained catalysts were recorded by field emission scanning electron microscopy (FE-SEM, HITACHIS-4800). The microstructures of the samples were recorded using high-resolution transmission electron microscopy (HRTEM, JOEL JEM 2100). UV–vis diffuse reflectance spectra (DRS) of the catalysts were acquired on a UV–vis spectrophotometer (UV-2550, Shimadzu) with an integrating sphere attachment within the wavelength range from 200 nm to 800 nm along with $BaSO_4$ as the reflectance standard. The photoluminescence (PL) emission spectra were carried out with an FLS920 fluorescence spectrometer at room temperature under the excitation wavelength of 300 nm.

2.4. Photocatalytic Degradation of RhB

The photocatalytic activities of as-obtained products determined by the degradation of RhB were conducted in a photoreaction apparatus, an XPA-II photochemical reactor (XPA-II, Nanjing Xujiang Machine-electronic Plant, China). In typical processing, a 30 mg catalyst was added to 30 mL of RhB solution (20 mg/L). The mixer was stirred for 30 min in the dark to achieve the adsorption–desorption equilibrium between the dye and the surface of the catalyst, then the reaction system was performed via the irradiation of a 300 W mercury lamp and by continuously stirring under favorable ambient conditions. At certain intervals of time, 4 mL of the mixed solution was collected and taken out for centrifugation to remove the catalyst and analyzed using a UV–vis spectrophotometer (UV-6100, Metash). The residual samples were collected for repeated photocatalytic reactions.

3. Results and Discussion

To know the phase composition of hetero photocatalyst, crystallinity, and purity, XRD was performed and is presented in Figure 1. The XRD pattern of $NaTaO_3$ shows that the peaks at 22.9°, 32.5°, 40.1°, 46.6°, 52.5°, 57.8°, 57.9°, and 67.9° are attributed to the (100), (101), (111), (200), ($\bar{1}$02), ($\bar{1}$12), ($\bar{1}$21), and (022) diffraction planes, respectively. All the diffraction peaks can be readily indexed as a pure perovskite $NaTaO_3$ with a monoclinic structure (JCPDS No. 74-2478) [10,12], which can facilitate the separation of photo-induced electron–hole pairs. As has been reported, $NaTaO_3$ may exist in three polymorphs, which are the orthorhombic, cubic, and monoclinic phases [10,12]. All the phases share TaO_6 octahedra frameworks at the corners, along with sodium ions residing in the dodecahedral interspaces, but the local structure distortion is highly different among various polymorphs [12]. The TaO_6 octahedra of the monoclinic phase were close to the ideal perovskite, favoring the separation of photo-induced electrons and holes and representing better photocatalytic activity [14]. After doping the S anion, it can also be seen that the diffraction peaks of NTO-S series samples still matched the monoclinic structure. As for bare Sn_3O_4, its XRD pattern showed poorer crystallinity and lower diffraction peak intensity. The principal diffraction peaks may correspond to the (101), ($\bar{1}$20), (111), ($\bar{2}$10), ($\bar{1}$21), and (210) crystal planes of standard triclinic-phase Sn_3O_4 (JCPDS No.16-0737) [29–31,34]. Additionally, the XRD patterns of Sn/NTO and Sn/NTO-S have no detected impurities, corresponding to the aforementioned $NaTaO_3$ and Sn_3O_4.
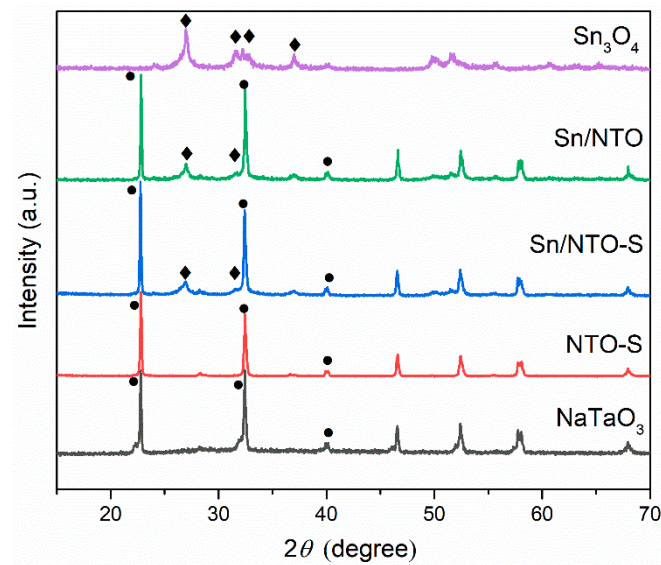
Figure 1. XRD patterns of as-obtained samples: $NaTaO_3$, NTO-S, Sn/NTO, Sn/NTO-S composites, and Sn_3O_4.

The morphologies and microstructural details of the as-prepared $NaTaO_3$, NTO-S, Sn/NTO, and Sn/NTO-S were discussed based on the SEM and TEM images. Figure 2 contains representative SEM images of the as-obtained samples. As shown (inset of Figure 2a,b), $NaTaO_3$ and NTO-S presented an approximate cubic structure with an average size between 300 nm and 500 nm, while the surfaces of some of them were a little coarse. Figure 2c,d shows the synthesized Sn_3O_4 clusters with low and high magnification, respectively, which are composed of thin flakes with a size range between 100 nm and 400 nm and a thickness of approximately 5–10 nm. Then the SEM images of Sn/NTO (Figure 2e) and Sn/NTO-S (Figure 2f) are displayed. Their surfaces were rough, which consisted of Sn_3O_4 nanoflakes and might provide still more active faces and a larger specific area beneficial to heterogeneous nucleation and assembly growth of Sn_3O_4 nanoflakes.

As shown in Figure 3a,b, $NaTaO_3$ always shows the cubic morphology before and after constructing with Sn_3O_4. Additionally, the average size of those composites changes little, approximately 300 nm. Evidently, the cubic $NaTaO_3$ was essentially surrounded by sheet-like Sn_3O_4 and a portion of small slices that were well dispersed on the outside surface of the cubic $NaTaO_3$ to compose a representative Sn/NTO heterojunction. Hence, Figure 3c illustrates a schematic diagram of the growth process of Sn/NTO in two steps. The first step is heterogeneous nucleation of Sn_3O_4 seeds on the outside surface of the cubic $NaTaO_3$, driven by the adsorption connecting -OH groups on the surface of the cubic $NaTaO_3$ with Sn^{2+} in the precursor [31]. The second step is Sn_3O_4 nanoflakes successfully growing an assembly on the outside surface of cubic $NaTaO_3$. The heterojunction between Sn_3O_4 and $NaTaO_3$ would facilitate photoresponse and interfacial electron transfer and therefore enhance the photocatalytic activity.
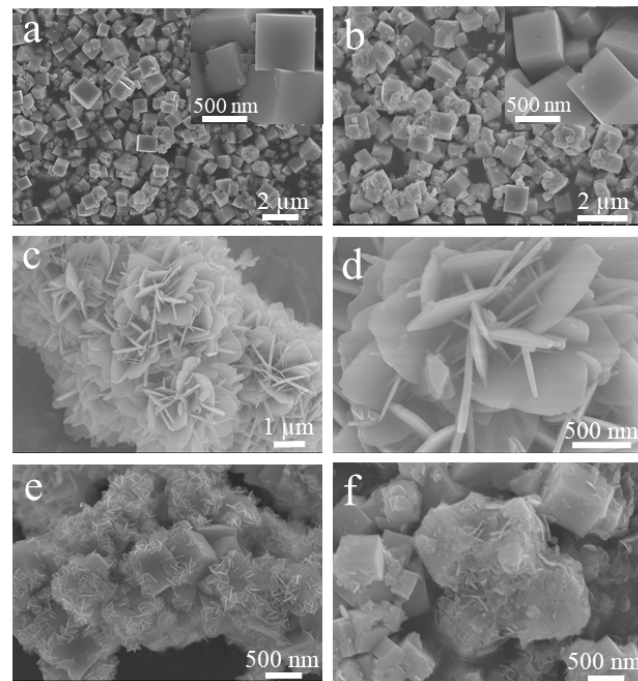
Figure 2. SEM images of NaTaO$_3$ (**a**), NTO-S (**b**), Sn$_3$O$_4$ (**c,d**), Sn/NTO composites (**e**), and Sn/NTO-S (**f**), respectively.
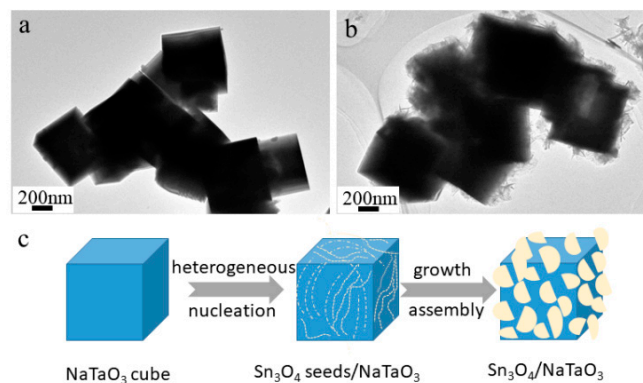

Figure 3. TEM images of NaTaO$_3$ (**a**), Sn/NTO (**b**), and a schematic diagram of the growth process of Sn/NTO (**c**).

The light properties of a material are very sensitive to and seriously influenced by their intrinsic microstructures and, therefore, any changes in electronic structure. Figure 4a determines the UV–vis diffuse reflectance spectra (DRS) of NaTaO$_3$, NTO-S, Sn/NTO, and Sn/NTO-S (molar ratio Sn/Ta = 1/1) heterostructures, along with pure Sn$_3$O$_4$. The bare NaTaO$_3$ presented steep absorption only in the UV region located at 308 nm. Sulfur ion doping in NaTaO$_3$ showed an intense absorption with an absorption red-shift of 323 nm. The pure Sn$_3$O$_4$ could absorb the light irradiation as its optical absorption was determined to be around 473 nm. After coupling NaTaO$_3$ or NTO-S, it was found that Sn/NTO and Sn/NTO-S heterostructures exhibited a broader absorption peak in contrast to pure NaTaO$_3$. The Sn/NTO composites presented a significant shift toward 484.7 nm. However, the Sn/NTO-S heterostructure showed a continuous red-shift to 523.5 nm. According to $hv = 1240/\lambda$ and the Kubelka–Munk (KM) method, with the equation: $\alpha hv = \text{A} \left(hv - E_g\right)^2$, in which α, hv, E_g, and A are the absorption coefficient, the photon energy, indirect bandgap, and a constant, respectively [10,11,31], the bandgap energies of NaTaO$_3$, NTO-S, Sn$_3$O$_4$, Sn/NTO, and Sn/NTO-S shown in Figure 4b were calculated to be 4.03 eV, 3.84 eV, 2.62 eV,

2.56 eV, and 2.37 eV, respectively. Hence, the bandgaps of the composites were greatly reduced. Interestingly, the bandgap values of Sn/NTO and Sn/NTO-S composites were not between pure NaTaO$_3$ and Sn$_3$O$_4$; the optical transitions of the composites extend much wider. Consequently, it can be inferred that the bandgap value of the composite narrowed via sulfur doping; then, the light absorption was further enhanced by coupling Sn$_3$O$_4$. The enhanced light response could be attributed to the formation of a heterojunction between them [10,11,18,26–29,31].
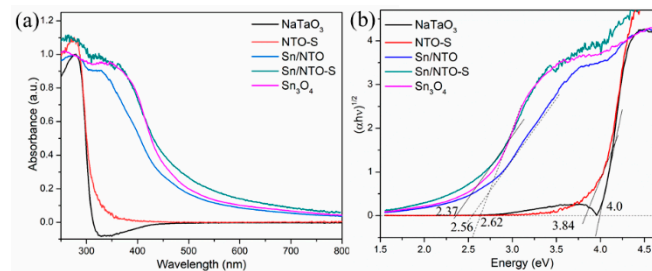

Figure 4. UV–vis diffuse reflectance spectra (DRS) (**a**) and the calculated band gaps (**b**) of different samples: NaTaO$_3$, NTO-S, Sn/NTO, Sn/NTO-S (molar ratio Sn:Ta = 1:1) heterostructure, and Sn$_3$O$_4$.

To investigate the photocatalytic degradation capabilities of the as-obtained catalysts, we carried out a degradation properties assessment using different samples on RhB in a photocatalytic device that had been specially designed. The degradation of RhB and the corresponding kinetic plots are displayed in Figure 5a,b, respectively. Figure 5a shows the different relative concentration variations of the RhB over 140 min. C_0 is the initial concentration of the RhB, and C_t is the concentration of the RhB after a reaction for *t*. The concentration of the RhB was almost constant, which implies that the RhB had attained the adsorption equilibrium in a short time and prior reaction. Therefore, it was confirmed that the decrease of RhB was a result of degradation as time went by. Cubic NaTaO$_3$ presented a steady degradation rate under UV light irradiation. After 120 min, the concentration of the RhB decreased by 63%. The photodegradation of the RhB in the presence of pure Sn$_3$O$_4$ performed relatively slowest, as only 18% of the RhB was degraded in the 120 min illumination period. The reduced degradation rate possibly contributed to the inhibited electron transportation efficiency and narrow spectral response in bare Sn$_3$O$_4$, which led to the fast recombination of photo-induced electron–hole pairs and poor activity. It is well known that NaTaO$_3$ exhibits low photocatalytic activity, even under UV illumination, due to its large bandgap. However, after having been doped in sulfur ion or coupled with Sn$_3$O$_4$, the photocatalytic degradation ability of NTO-S or Sn/NTO was very much enhanced in contrast to that of the pure NaTaO$_3$ or the Sn$_3$O$_4$ catalyst. Interestingly, both displayed similar photocatalytic degradation rates of RhB under UV light irradiation. The Sn/NTO-S showed the best performance. The RhB was degraded almost entirely in 120 min, which also demonstrated that heterojunction structure plays a decisive role in the transportation and separation of photo-induced carriers.
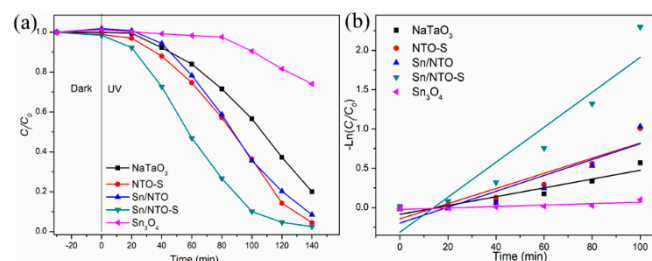

Figure 5. Photocatalytic degradation activities (**a**) and plots (**b**) of –Ln (C_t/C_0) vs. irradiation time for RhB degradation under ultraviolet light irradiation, measured at regular time intervals in the presence of NaTaO$_3$, NTO-S, Sn/NTO, Sn/NTO-S, and Sn$_3$O$_4$, respectively.

Furthermore, the degradation rate for RhB can be acquired from the slope (min^{-1}) of $-Ln(C_t/C_0) \sim t$ plots (Figure 5b); the calculated results of the decolorization rate constant κ (min^{-1}) for NaTaO$_3$, NTO-S, Sn/NTO, Sn/NTO-S, and Sn$_3$O$_4$ were 0.3366, 0.5790, 0.6060, 1.3350, and 0.0555 min^{-1}, respectively. Evidently, the Sn/NTO-S catalyst exhibited the highest κ values (1.3550 min^{-1}), which were about 4.0 times those of NaTaO$_3$.

Based on the experimental results mentioned above, a schematic model of a proposed reaction pathway of degraded products is illustrated in Scheme 1. The band edge positionings of NaTaO$_3$ and Sn$_3$O$_4$ were carefully made based on experimental results and earlier studies. Via DRS, the bandgap energy of NaTaO$_3$ (4.03 eV) was wider than that of Sn$_3$O$_4$ (2.62 eV) [38]. The CB of NaTaO$_3$ was estimated to be −0.99 eV, as documented [10,39]. The narrowing of bandgap energy as a result of doping S anion is a very key factor. The photodegradation efficiency of NTO-S was found to be greater than that of pure NaTaO$_3$. The reason may be that the substitution of resident O atoms within the NaTaO$_3$ lattice by sulfur atoms induced the local states just above the valence level as the new hybridized orbitals were formed [12,40]. Aside from the bandgap width, the photocatalytic degradation activity of a sample highly depended on the recombination of electron (e$^-$)–hole (h$^+$) pairs [12,41–44]. Under photo-irradiation, the photo-induced e−/h+ pairs on the CB/VB of each semiconductor were created. As reported previously, the principal active species for the photocatalytic degradation of RhB included hydroxyl radicals (●OH) and superoxide radicals (●O$_2^-$), which were composed of the creation of h$^+$ and e$^-$ [34], and some researchers have explored intermediates and key reaction species [45–47]. S-doped catalysts displayed a less intense emission than pure NaTaO$_3$ samples, indicating a reduced e$^-$/h$^+$ recombination and an enhanced RhB photodegradation performance [12].
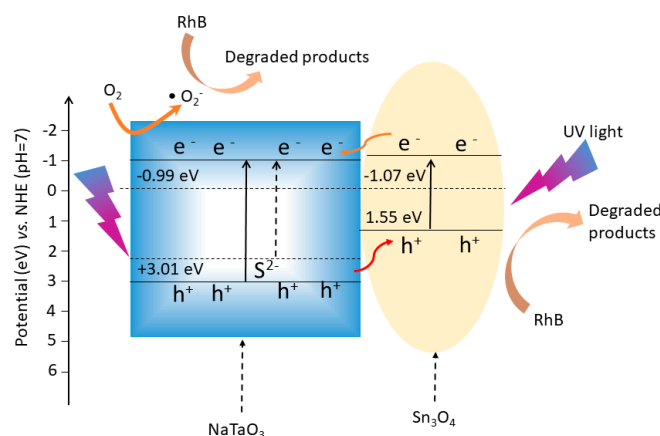
Scheme 1. Schematic model of a proposed reaction pathway of degraded products.

This plausible mechanism comprised excitation of the CB of the Sn$_3$O$_4$; then, the e$^-$ on the CB of the NaTaO$_3$ reacted with the available O$_2$ to produce the superoxide radicals ●O$_2^-$. Then, the ●O$_2^-$ degraded RhB, or the RhB intermediate, into degraded products [45]. The h$^+$ of the NTO-S transmitted to the VB of the Sn$_3$O$_4$ [31], and holes contributed more to the high photocatalytic performance, while ●OH showed less importance in its ability to degrade RhB [34]. In this case, the RhB reacted with h$^+$ and formed the intermediate RhB that was finally converted to degraded products. Comprehensively, the photocatalytic degradation mechanisms could be depicted as the interfacial charge transfer of the composite-enhanced RhB photosensitization process under irradiation, which could effectively separate and transfer photogenerated carriers. Therefore, the resultant ●O$_2^-$ and h$^+$ favored the photodegradation procedure, and the coupled semiconducting materials formed more dynamic catalytic centers that improved the efficiency of RhB dye removal. This suggested that high-quality interfaces in the heterostructure composites played a vital role in enhancing the catalytic performance.

To prove the rationality of the proposed reaction pathway and investigate the capabilities of photo-induced e−/h+ pairs in the semiconductors, PL emission spectra of NaTaO$_3$, NTO-S, Sn/NTO, Sn/NTO-S, and Sn$_3$O$_4$ were carried out, respectively. PL emission arises from the recombination of free carriers, and a higher PL intensity reveals a higher recombination rate of photogenerated e−/h+ pairs. By contrast, a weaker PL intensity indicates a lower recombination rate of photo-excited e−/h+ pairs, and accordingly, much more photo-induced carriers can participate in the photocatalytic reaction [10,34]. As shown in Figure 6, the spectrum of NaTaO$_3$ nanocubes showed three peaks at around 395 nm, 451 nm, and 469 nm. The emission at 451 nm and 469 nm was due to band-to-band mixing of Ta^{4+}-O$^−$ states in the octahedral TaO$_6$ motifs of NaTaO$_3$ [48]. After doping the S anion in NaTaO$_3$, the PL intensity of NTO-S was weaker than that of pure NaTaO$_3$. It indicated that the NTO-S could suppress the recombination of e−/h+ pairs. Noticeably, the intensities of the PL spectra of Sn/NTO and the Sn/NTO-S heterojunction photocatalysts strongly decreased with the Sn/NTO heterojunctions formed as compared to pure cubic NaTaO$_3$; this can be seen at the maximum PL intensity at around 469 nm. The lower PL intensity implied the efficient inhibition of photogenerated pairs and therefore higher photocatalytic activity in the UV light region, which could effectively explain the variation of the photocatalytic activities of the different samples.
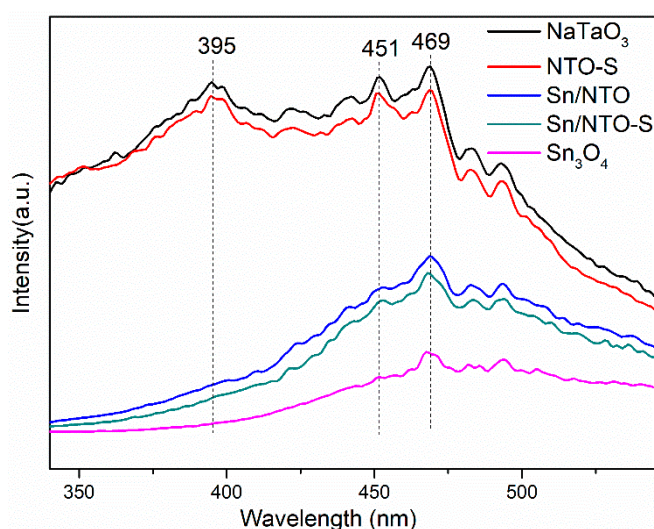

Figure 6. Room temperature photoluminescence (PL) spectra of NaTaO$_3$, NTO-S, Sn/NTO, Sn/NTO-S, and Sn$_3$O$_4$, respectively.

4. Conclusions

On the whole, we have successfully synthesized a novel Sn$_3$O$_4$/NaTaO$_3$ heterojunction with doping sulfur anion via a simple hydrothermal method. The bandgap value of NaTaO$_3$ and the composite narrowed via sulfur doping, which induced an increase in light absorption. With coupling Sn$_3$O$_4$, it was found that the as-obtained Sn/NTO and Sn/NTO-S composites exhibited cubic NaTaO$_3$, or that NTO-S assembled by countless interlaced fine Sn$_3$O$_4$ nanoflakes were successfully synthesized for the first time. The fabrication of enough interfaces with high qualities played a critical role in light absorption and enhancing photocatalytic performance. Assessed by the degradation of the RhB solution, the Sn/NTO-S composite presents a superior photoreactivity toward RhB degradation under UV light illumination in contrast to individual Sn$_3$O$_4$ or NaTaO$_3$. The calculated decolorization rate constant is much greater (1.3550 min^{-1}) than single Sn$_3$O$_4$ (0.0555 min^{-1}) or NaTaO$_3$ (0.3366 min^{-1}). This could be due to the enhanced light absorbance by the larger specific surface area of the Sn$_3$O$_4$ nanoflakes and the formation of the heterojunction between NTO-S and Sn$_3$O$_4$, which can separate photo-induced carriers efficiently. It is also proposed that the formed ●O$_2^−$ and h$^+$ favored the photocatalytic degradation of RhB. This

work highlights the importance of heterostructured Sn_3O_4/$NaTaO_3$, which may provide a lead to develop high potential and $NaTaO_3$-based photocatalysts for the degradation of organic dyes.

Author Contributions: Conceptualization, S.C. and H.L.; methodology, S.C.; software, Y.S.; validation, S.C. and Y.S.; formal analysis, S.C.; investigation, S.C.; resources, Y.S.; data curation, Y.S.; writing—original draft preparation, S.C.; writing—review and editing, S.C.; visualization, Y.S.; supervision, H.L.; project administration, H.L.; funding acquisition, S.C. All authors have read and agreed to the published version of the manuscript.

Institutional Review Board Statement: Not applicable.

Informed Consent Statement: Not applicable.

Conflicts of Interest: The authors declare no conflict of interest.

References

1. Akbal, F. Photocatalytic degradation of organic dyes in the presence of titanium dioxide under UV and solar light: Effect of operational parameters. *Env. Prog.* **2005**, *24*, 317–322. [CrossRef]
2. Schneider, J.; Matsuoka, M.; Takeuchi, M.; Zhang, J.; Horiuchi, Y.; Anpo, M.; Bahnemann, D.W. Understanding TiO_2 photocatalysis: Mechanisms and materials. *Chem. Rev.* **2014**, *114*, 9919–9986. [CrossRef] [PubMed]
3. Yang, J.; Wang, D.; Han, H.; Li, C. Roles of Cocatalysts in Photocatalysis and Photoelectrocatalysis. *Acc. Chem. Res.* **2013**, *46*, 1900–1909. [CrossRef] [PubMed]
4. Matatov-Meytal, Y.I.; Sheintuch, M. Catalytic Abatement of Water Pollutants. *Ind. Eng. Chem. Res.* **1998**, *37*, 309–326. [CrossRef]
5. Kabra, K.; Chaudhary, R.; Sawhney, R.L. Treatment of Hazardous Organic and Inorganic Compounds through Aqueous-Phase Photocatalysis: A Review. *Ind. Eng. Chem. Res.* **2004**, *43*, 7683–7696. [CrossRef]
6. Chang, S.; Yang, X.; Sang, Y.; Liu, H. Highly Efficient Photocatalysts and Continuous-Flow Photocatalytic Reactors for Degradation of Organic Pollutants in Wastewater. *Chem. Asian J.* **2016**, *11*, 2352–2371. [CrossRef] [PubMed]
7. Chang, S.; Wang, Q.; Liu, B.; Sang, Y.; Liu, H. Hierarchical TiO_2 nanonetwork–porous Ti 3D hybrid photocatalysts for continuous-flow photoelectrodegradation of organic pollutants. *Catal. Sci. Technol.* **2017**, *7*, 524–532. [CrossRef]
8. Someshwar Pola and Ramesh Gade. Significant Role of Perovskite Materials for Degradation of Organic Pollutants. Available online: https://www.intechopen.com/online-first/significant-role-of-perovskite-materials-for-degradation-of-organic-pollutants (accessed on 3 April 2020).
9. Orak, C.; Atalay, S.; Ersöz, G. Photocatalytic and photo-Fenton-like degradation of methylparaben on monolith-supported perovskite-type catalysts. *Sep. Sci. Technol.* **2017**, *52*, 1310–1320. [CrossRef]
10. Xu, J.; Luo, B.; Gu, W.; Jian, Y.; Wu, F.; Tang, Y.; Shen, H. Fabrication of In_2S_3/$NaTaO_3$ composites for enhancing the photocatalytic activity toward the degradation of tetracycline. *New J. Chem.* **2018**, *42*, 5052–5058. [CrossRef]
11. Qu, L.; Lang, J.; Wang, S.; Chai, Z.; Su, Y.; Wang, X. Nanospherical composite of WO_3 wrapped $NaTaO_3$: Improved photodegradation of tetracycline under visible light irradiation. *Appl. Surf. Sci.* **2016**, *388*, 412–419. [CrossRef]
12. Li, H.; Shi, X.; Liu, X.; Li, X. Synthesis of novel, visible-light driven S,N-doped $NaTaO_3$ catalysts with high photocatalytic activity. *Appl. Surf. Sci.* **2020**, *508*, 145306. [CrossRef]
13. Kato, H.; Kudo, A. Highly efficient decomposition of pure water into H_2 and O_2 over $NaTaO_3$ photocatalysts. *Catal. Lett.* **1999**, *58*, 153–155. [CrossRef]
14. Hu, C.; Tsai, C.; Teng, H. Structure Characterization and Tuning of Perovskite-Like $NaTaO_3$ for Applications in Photoluminescence and Photocatalysis. *J. Am. Ceram. Soc.* **2009**, *92*, 460–466. [CrossRef]
15. An, L.; Sasaki, T.; Weidler, P.G.; Wöll, C.; Ichikuni, N.; Onishi, H. Local Environment of Strontium Cations Activating $NaTaO_3$ Photocatalysts. *ACS Catal.* **2018**, *8*, 880–885. [CrossRef]
16. He, Y.; Zhu, Y.; Wu, N. Synthesis of nanosized $NaTaO_3$ in low temperature and its photocatalytic performance. *J. Solid State Chem.* **2004**, *177*, 3868–3872. [CrossRef]
17. An, L.; Onishi, H. Electron–Hole Recombination Controlled by Metal Doping Sites in NaTaO3 Photocatalysts. *ACS Catal.* **2015**, *5*, 3196–3206. [CrossRef]
18. Yang, F.; Yan, L.; Zhang, B.; He, X.; Li, Y.; Tang, Y.; Ma, C.; Li, Y. Fabrication of ternary $NaTaO_3$/g-C_3N_4/G heterojunction photocatalyst with enhanced activity for Rhodamine B degradation. *J. Alloys Compd.* **2019**, *805*, 802–810. [CrossRef]

19. Zhou, X.; Chen, Y.; Mei, H.; Hu, Z.; Fan, Y. A facile route for the preparation of morphology-controlled NaTaO$_3$ films. *Appl. Surf. Sci.* **2008**, *255*, 2803–2807. [CrossRef]

20. Torresmartinez, L.M.; Cruzlopez, A.; Juarezramirez, I.; Meza-de la Rosa, M.E. Methylene blue degradation by NaTaO$_3$ sol-gel doped with Sm and La. *J. Hazard. Mater.* **2009**, *165*, 774–779. [CrossRef]

21. Kato, H.; Asakura, A.K.; Kudo, A. Highly Efficient Water Splitting into H$_2$ and O$_2$ over Lanthanum-Doped NaTaO$_3$ Photocatalysts with High Crystallinity and Surface Nanostructure. *J. Am. Chem. Soc.* **2003**, *125*, 3082–3089. [CrossRef]

22. Iwase, A.; Kato, H.; Kudo, A. The Effect of Alkaline Earth Metal Ion Dopants on Photocatalytic Water Splitting by NaTaO$_3$ Powder. *ChemSusChem* **2009**, *2*, 873–877. [CrossRef] [PubMed]

23. Liu, D.; Jiang, Y.; Gao, G. Photocatalytic degradation of an azo dye using N-doped NaTaO$_3$ synthesized by one-step hydrothermal process. *Chemosphere* **2011**, *83*, 1546–1552. [CrossRef] [PubMed]

24. Wang, M.; Ma, Y.; Fo, Y.; Lyu, Y.; Zhou, X. Theoretical insights into the origin of highly efficient photocatalyst NiO/NaTaO$_3$ for overall water splitting. *Int. J. Hydrogen Energy* **2020**, *45*, 19357–19369. [CrossRef]

25. Xu, D.; Shi, W.; Yang, S.; Chen, B.; Bai, H.; Xiao, L. Fabrication of ternary p-n heterostructures AgCl/Ag$_2$O/NaTaO$_3$ photocatalysts: Enhanced charge separation and photocatalytic properties under visible light irradiation. *Catal. Commun.* **2016**, *84*, 163–166. [CrossRef]

26. Tang, L.; Feng, C.; Deng, Y.; Zeng., G.; Wang, J.; Liu, Y.; Feng, H.; Wang, J. Enhanced photocatalytic activity of ternary Ag/g-C$_3$N$_4$/NaTaO$_3$ photocatalysts under wide spectrum light radiation: The high potential band protection mechanism. *Appl. Catal. B Environ.* **2018**, *230*, 102–114. [CrossRef]

27. Gomezsolis, C.; Ballesteros, J.C.; Torresmartinez, L.M.; Juárez-Ramírez, I. RuO$_2$–NaTaO$_3$ heterostructure for its application in photoelectrochemical water splitting under simulated sunlight illumination. *Fuel* **2016**, *166*, 36–41. [CrossRef]

28. Singh, A.P.; Kumar, S.; Thirumal, M. Efficient Charge Transfer in Heterostructures of CdS/NaTaO$_3$ with Improved Visible-Light-Driven Photocatalytic Activity. *ACS Omega* **2019**, *4*, 12175–12185. [CrossRef]

29. Xia, W.; Wang, H.; Zeng, X.; Han, J.; Zhu, J.; Zhou, M.; Wu, S. High-efficiency photocatalytic activity of type II SnO/Sn$_3$O$_4$ heterostructures via interfacial charge transfer. *CrystEngComm* **2014**, *16*, 6841–6847. [CrossRef]

30. He, Y.; Li, D.; Chen, J.; Shao, Y.; Xian, J.; Zheng, X.; Wang, P. Sn$_3$O$_4$: A novel heterovalent-tin photocatalyst with hierarchical 3D nanostructures under visible light. *Rsc Adv.* **2014**, *4*, 1266–1269. [CrossRef]

31. Chen, G.; Ji, S.; Sang, Y.; Chang, S.; Wang, Y.; Hao, P.; Claverie, J.; Liu, H.; Yu, G. Synthesis of scaly Sn$_3$O$_4$/TiO$_2$ nanobelt heterostructures for enhanced UV-visible light photocatalytic activity. *Nanoscale* **2015**, *7*, 3117–3125. [CrossRef]

32. Park, S.H.; Son, Y.C.; Willis, W.S.; Suib, S.L.; Creasy, K.E. Tin oxide films made by physical vapor deposition thermal oxidation and spray pyrolysis. *Chem. Mater.* **1998**, *10*, 2389–2398. [CrossRef]

33. Yu, X.; Zhao, Z.; Ren, N.; Liu, J.; Sun, D.; Ding, L.; Liu, H. Top or Bottom, Assembling Modules Determine the Photocatalytic Property of the Sheetlike Nanostructured Hybrid Photocatalyst Composed with Sn$_3$O$_4$ and rGO (GQD). *ACS Sustain. Chem. Eng.* **2018**, *6*, 11775–11782. [CrossRef]

34. Hu, J.; Li, X.; Wang, X.; Li, Q.; Wang, F. Novel hierarchical Sn$_3$O$_4$/BiOX (X = Cl, Br, I) p–n heterostructures with enhanced photocatalytic activity under simulated solar light irradiation. *Dalton Trans.* **2019**, *48*, 8937–8947. [CrossRef] [PubMed]

35. Yu, H.; Li, J.; Luo, W.; Li, Z.; Tian, Y.; Yang, Z.; Gao, Z.; Liu, H. Hetero-structure La$_2$O$_3$-modified SnO$_2$-Sn$_3$O$_4$ from tin anode slime for highly sensitive and ppb-Level formaldehyde detection. *Appl. Surf. Sci.* **2020**, *513*, 145825. [CrossRef]

36. Manikandan, M.; Tanabe, T.; Li, P.; Ueda, S.; Ramesh, G.V.; Kodiyath, R. Photocatalytic Water Splitting under Visible Light by Mixed-Valence Sn$_3$O$_4$. *ACS Appl. Mater. Interfaces* **2014**, *6*, 3790–3793. [CrossRef] [PubMed]

37. Hu, J.; Tu, J.; Li, X.; Wang, Z.; Li, Y.; Li, Q.; Wang, F. Enhanced UV-Visible Light Photocatalytic Activity by Constructing Appropriate Heterostructures between Mesopore TiO$_2$ Nanospheres and Sn$_3$O$_4$ Nanoparticles. *Nanomaterials* **2017**, *7*, 336. [CrossRef]

38. Portugal, G.R.; Santos, S.F.; Arantes, J.T. NaTaO$_3$ cubic and orthorhombic surfaces: An intrinsic improvement of photocatalytic properties. *Appl. Surf. Sci.* **2020**, *502*, 144206. [CrossRef]

39. Modak, B.; Srinivasu, K.; Ghosh, S.K. Band gap engineering of NaTaO$_3$ using density functional theory: A charge compensated codoping strategy. *Phys. Chem. Chem. Phys.* **2014**, *16*, 17116–17124. [CrossRef]

40. Li, F.; Liu, D.; Gao, G.; Xue, B.; Jiang, Y. Improved visible-light photocatalytic activity of NaTaO$_3$ with perovskite-like structure via sulfur anion doping. *Appl. Catal. B Environ.* **2015**, *166*, 104–111. [CrossRef]

41. Li, Z.; Ma, B.; Zhang, X.; Sang, Y.; Liu, H. One-pot synthesis of BiOCl nanosheets with dual functional carbon for ultra-highly efficient photocatalytic degradation of RhB. *Environ. Res.* **2020**, *182*, 109077. [CrossRef]

42. Alido, J.P.M.; Sari, F.N.I.; Ting, J.-M. Synthesis of Ag/hybridized 1T-2H MoS$_2$/TiO$_2$ heterostructure for enhanced visible-light photocatalytic activity. *Ceram. Int.* **2019**, *45*, 23651–23657. [CrossRef]

43. Sari, F.N.I.; Lu, S.-H.; Ting, J.-M. Wide-bandgap HfO$_2$-V$_2$O$_5$ nanowires heterostructure for visible light driven photocatalytic degradation. *J. Am. Ceram. Soc.* **2020**, *103*, 2252–2261. [CrossRef]

44. Sari, F.N.I.; Yen, D.T.K.; Ting, J.-M. Enhanced photocatalytic performance of TiO$_2$ through a novel direct dual Z-scheme design. *Appl. Surf. Sci.* **2020**, *533*, 147506. [CrossRef]

45. Munusamy, T.D.; Yee, C.S.; Khan, M.M.R. Construction of hybrid g-C$_3$N$_4$/CdO nanocomposite with improved photodegradation activity of RhB dye under visible light irradiation. *Adv. Powder Technol.* **2020**, *31*, 2921–2931. [CrossRef]

46. Zhang, Z.; Feng, Y.; Liu, N.; Zhao, Y.; Wang, X.; Yang, S.; Long, Y.; Qiu, L. Preparation of Sn/Mn loaded steel slag zeolite particle electrode and its removal effect on rhodamine B(RhB). *J. Water Process Eng.* **2020**, *37*, 101417. [CrossRef]
47. Ding, X.; Gutierrez, L.; Croue, J.-P.; Li, M.; Wang, L.; Wang, Y. Hydroxyl and sulfate radical-based oxidation of RhB dye in UV/H$_2$O$_2$ and UV/persulfate systems: Kinetics, mechanisms, and comparison. *Chemosphere* **2020**, *253*, 126655. [CrossRef]
48. Lee, Y.C.; Teng, H.; Hu, C.C.; Hu, S.Y. Temperature-dependent photoluminescence in NaTaO$_3$ with different crystalline structures. *Electrochem. Solid State Lett.* **2008**, *11*, P1–P4. [CrossRef]